RESEARCH

Study on the properties of alkali-activated phosphorus slag mortar mixed with granulated blast furnace slag/fly ash

Yannian Zhang[1] · Qi Wu[1] · Daokui Yang[1] · Qingjie Wang[2] · Zhifu Qu[3] · Yugang Zhong[3]

Abstract

Alkali-activated materials (AAMs), which are prepared by using various solid wastes as precursors and reacting with alkaline solutions, are gradually applied in the construction industry. However, not all solid waste precursors can exhibit good performance in the preparation of AAMs. To realize the effective utilization of phosphorus slag (PS) solid waste, alkali-activated PS-GBFS-FA (AAPGF) was prepared by using PS and GBFS/FA. Using different contents of GBFS/FA to replace PS, the workability performance, mechanical properties and hydration products of AAPGF were investigated. The incorporation of GBFS/FA improves the fluidity of AAPGF, but leads to slurry flash setting. When containing 30% GBFS/FA, the 28 days compressive strength of AAPGF can reach the highest 72.65 MPa. GBFS/FA increased the number of C-(A)-S-H gels, accompanied by the formation of hydrotalcite gels. In addition, GBFS/FA also transforms AAPGF hydration products from C-S-H gel to C-(N)-A-S-H and N-A-S-H gel with high degree of polymerization, and SiO_4 tetrahedron is Q^2 unit. GBFS/FA will significantly reduce unhydrated particles, but it will lead to uneven distribution of hydration products and produce large pores. The results of this study can provide reference value for the effective use of PS.

Keywords Alkali-activated materials · Phosphorus slag · Workability performance · Compressive strength · Hydration products

Introduction

In the process of modern social development, a large amount of ordinary Portland cement (OPC) is consumed every day for the construction of various infrastructures. According to statistics, OPC production is growing at a rate of 9% per year worldwide [1]. The OPC production process, not only consumes mineral resources and fossil energy but also produces a large amount of greenhouse gases [2]. The study found that the CO_2 content emitted for the production of OPC accounts for 8% of global anthropogenic CO_2 emissions, and this proportion is still growing [3, 4]. Such a huge amount of carbon emissions will aggravate environmental damage and is not conducive to the sustainable development currently advocated. In this context, alkali-activated materials (AAMs) with low energy consumption and carbon emissions have attracted people's attention.

AAMs are new cementitious materials formed by the reaction of alkali activators and precursors rich in silicon and aluminum [5]. The most common use of alkali activators is NaOH, Na_2SiO_3 and Na_2CO_3 or a combination of the three [6, 7]. The precursors for the preparation of AAMs are mostly composed of industrial solid waste (e.g., granulated blast furnace slag (GBFS) [8], fly ash (FA) [9], steel slag [10]) and mine solid waste (e.g., coal gangue [11], bauxite [12]). Compared with OPC, AAMs can not only significantly reduce carbon emissions and energy consumption [6], but also help to absorb various types of solid waste. In addition, AAMs also have many excellent properties such as good compressive strength [13], excellent durability [14], heavy metal adsorption capacity [15], fire resistance [16], and are considered to be one of the ideal substitutes for OPC.

Phosphorus slag (PS) is a by-product produced during the extraction of yellow phosphorus. Globally, large amounts

✉ Qi Wu
WQ18341833149@stu.sjzu.edu.cn

1   School of Civil Engineering, Shenyang Jianzhu University, 110168 Shenyang, China

2   School of Science, Shenyang Jianzhu University, 110168 Shenyang, China

3   China Railway Construction Bridge Engineering Bureau Group 4th Engineering Co. Ltd, 150008 Harbin, China

of PS are emitted every year, with China alone emitting more than 8 million tons a year [17, 18]. Due to the lack of effective treatment methods, these PS are often directly accumulated outdoors, occupying land, and causing toxic ions to penetrate the soil under rainwater erosion, causing environmental pollution [19]. Thus, PS recycling is of great importance. PS consists primarily of calcium oxide (CaO) and silica (SiO_2), with a small amount of alumina (Al_2O_3) and phosphorus pentoxide (P_2O_5) present, and the content of the amorphous phase is greater than 90% [20], indicating that it has potential reactivity and can be used to prepare AAMs. However, due to the presence of phosphorus and fluorine in PS, the early hydration of the slurry is hindered, and the lower Al_2O_3 content also makes the activity of PS lower than that of GBFS [21]. To this end, some scholars have tried to use different methods to improve the activity of alkali-activated phosphorus slag (AAPS). Xie et al. [19] found that high alkali concentration conditions can accelerate the dissolution rate of AAPS and increase the number of hydration products. Jia et al. [22] found that increasing the alkali concentration can increase the early strength of AAPS, but it affects the compactness of the matrix in the later stage, which has a negative effect on the strength. Maghsoodloo-rad et al. [23] found that the compressive strength of AAPS can be increased by more than twice when the curing temperature of AAPS is increased from 25 °C to 90 °C under the same curing time. It is not difficult to see from the above results that the performance of AAPS depends on high temperature and high alkaline concentration to get play. However, this undoubtedly hinders the application of PS as AAMs precursor.

FA and GBFS are industrial by-products emitted from power plants and ironworks, respectively [24, 25]. Their chemical composition contains active silicon-oxygen-aluminum components, which are the two most commonly used precursor materials for AAMs. AAMs prepared with GBFS/FA as a precursor can exhibit good workability performance, mechanical properties and durability at room temperature [26, 27]. Moreover, when GBFS/FA is combined with some inert precursor materials to prepare AAMs, it can synergistically hydrate and improve its performance. Sun et al. [28] prepared AAMs by using solid waste white mud (mainly composed of calcium carbonate) produced by the papermaking industry as a filler and GBFS/FA together. The results show that the 28 days strength is better than that of OPC slurry even when the content of white mud in the slurry reaches 50%, and it also has better early strength.

Huseien et al. [29] replaced GBFS/FA with waste ceramic powder in a ratio of 50–70% to prepare AAMs with a 28-day compressive strength greater than 70 MPa. Song et al. [30] prepared AAMs by replacing FA with steel slag and GBFS in a certain proportion, and found that the amorphous gel of AAMs containing steel slag increased and the porosity decreased.

In addition to PS, other solid waste materials also have problems of poor workability or mechanical properties when they are used as precursors to prepare AAMs alone [31, 32]. It is considered to be the best way to solve this problem by using the synergistic coupling between different materials as precursors to improve each other's performance [33]. Therefore, to realize the effective utilization of PS, alkali-activated PS-GBFS-FA (AAPGF) was prepared by using PS and GBFS/FA as precursors. The workability performance, mechanical properties and hydration products of AAPGF were investigated by replacing PS with different contents of GBFS/FA. The synergistic effect between GBFS/FA and PS was used to overcome the problem that AAPS was difficult to be effectively applied at room temperature and normal alkaline concentration. This paper makes up for the blank of PS and GBFS/FA as precursors to prepare AAMs, and also provides some reference value for the utilization of PS in AAMs.

Materials and methodology

Materials

The test PS was taken from Kunming Haifu Trading Co., Ltd (Yunnan Province, China), GBFS from Jiyuan Steel Mill (Henan Province, China), FA was taken from Yatai Co., Ltd (Liaoning Province, China). According to Table 1, PS and GBFS mainly contain calcium oxide (CaO), silica (SiO_2) and alumina (Al_2O_3), PS exhibits a lower Al_2O_3 content and contains a small amount of phosphorus pentoxide (P_2O_5). FA is primarily composed of SiO_2 and Al_2O_3, followed by CaO and iron oxide (Fe_2O_3). The particle size distribution was shown in Fig. 1. The median particle sizes (D50) of PS, GBFS and FA were 20.52 μm, 10.60 μm and 8.92 μm, respectively. The scanning electron microscopy (SEM) results of PS, GBFS and FA particles are shown in Fig. 2. PS and GBFS are irregularly angular, while FA is mostly spherical and a few are irregular. Figure 3 is the X-ray diffraction (XRD) test results. The image shows that both PS

Table 1 Chemical composition and content of materials (wt%)

Materials	CaO	SiO_2	Al_2O_3	MgO	Fe_2O_3	K_2O	Na_2O	P_2O_5
PS	47.45	39.08	3.94	2.90	1.14	0.87	0.60	2.34
GBFS	42.26	30.73	15.96	6.66	0.29	0.34	0.04	–
FA	4.01	53.97	31.15	1.01	4.16	2.04	0.88	–
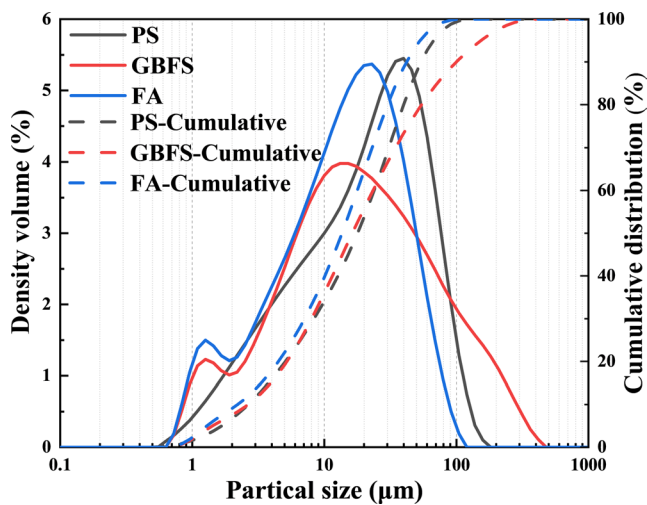
Fig. 1 Particle size distribution of raw materials

Fig. 3 XRD patterns of raw materials

and GBFS have a large hump at 20–40° 2θ, which suggests the raw materials contain amorphous aluminosilicate compounds [20, 34]. There are calcite, quartz and magnesium oxide in the crystal phase of PS. The crystal phase of GBFS is mainly consist of gehlenite, dicalcium silicate and calcite. The phase of FA is mainly composed of mullite, quartz and a small amount of hematite, magnetite and other crystal phases, and the content of amorphous phase is low. The more crystal phase of FA is the reason for its weak hydration activity [24]. However, this characteristic proves beneficial in mitigating the swift condensation of GBFS, establishing a favorable coupling effect [27]. The standard sand for the test was taken from Xiamen City, Fujian Province, the particle size distribution and XRD analysis are shown in Ref [35]. The NaOH from Kemao Co., Ltd (Tianjin, China), with a purity of more than 96%. Na_2SiO_3 was obtained from Gongyi Borun Refractories Co., Ltd (Henan Province, China). The purity of Na_2SiO_3 is more than 98.5% and the modulus is 2 M. The two solutions were mixed as an activator.

Sample preparation

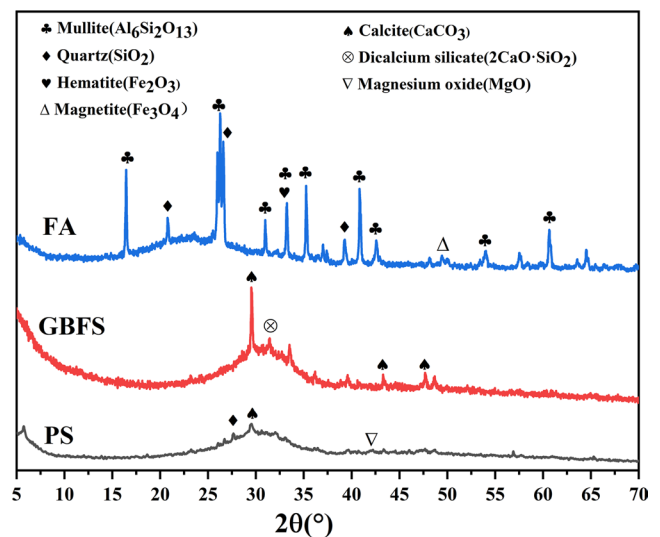Alkali-activated PS-GBFS-FA (AAPGF) was prepared by replacing PS with GBFS/FA in the ratio of 30%, 40% and

50% denoted as PFG-0–PGF-3 based on varying GBFS/FA masses. In the precursor materials of AAPGF, since both PS and GBFS are high calcium materials, excessive calcium content has an adverse effect on the workability of AAMs [34]. To optimize the element content in the system, the GBFS content in GBFS/FA is kept unchanged, and the FA content is increased (accounting for 10–30% of the total mass of the cementitious material).

Alkali activator is an important part of AAMs. Caldas et al. [32] and Marvila et al. [36] found that the type of alkali activator and sodium content have an important influence on the performance of AAMs. Therefore, according to the previous research of the research group [37], NaOH and Na_2SiO_3 were used as composite alkali activators, and the modulus was fixed at 1.5, and the water-binder ratio was 0.35. The specific ratio is shown in Table 2. Notably, the negligible Na_2O content in GBFS/FA (Table 1) renders the impact of its addition on the alkali concentration in the reaction inconsequential. The treated materials were poured into the mixer according to GB/T 17,671–2021 for preparation. Subsequently, the stirred slurry was injected into the 40 mm × 40 mm × 160 mm steel mold twice. Initially, approximately half of the slurry was injected and vibration
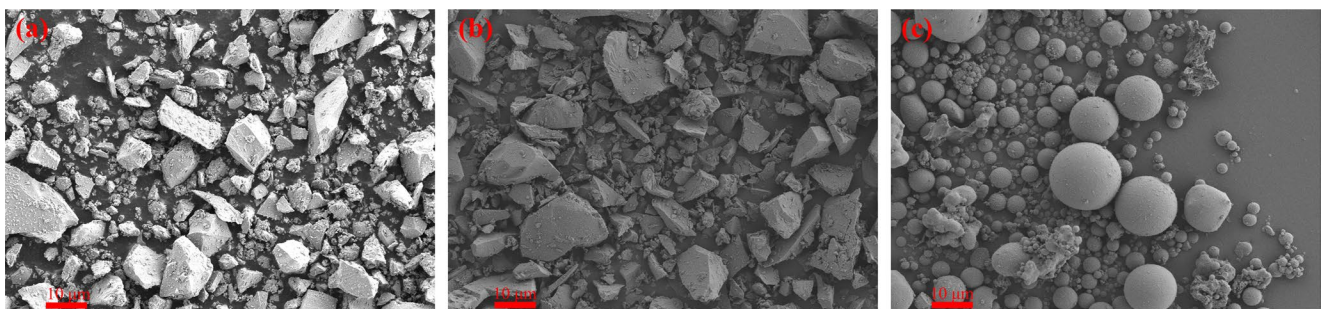

Fig. 2 SEM images of raw materials: (a) PS, (b) GBFS, and (c) FA

Table 2 Mix design (g)

Samples	PS	GBFS	FA	Standard Sand	NaOH	Na_2SiO_3	Water
PGF-0	450	0	0	1350	9.1	66.37	157.5
PGF-1	315	90	45	1350	9.1	66.37	157.5
PGF-2	270	90	90	1350	9.1	66.37	157.5
PGF-3	225	90	135	1350	9.1	66.37	157.5

Fig. 4 Fluidity test process

commenced. After the compaction, the remaining slurry is filled into the mold to start the second compaction. After the compaction is completed, the surface is flattened with a scraper. Curing to the specified age at a temperature of 20 ± 1 °C and RH$\geq$95%.

Test methods

Workability

The fluidity test, conducted in accordance with GB/T 2419–2005, utilized NLD-3 type jump table (China, Zhejiang Dadi Instrument Co., Ltd.) for testing. The mixed slurry was poured into a mold placed on the flow table and tamp with a tamper. Subsequently, the mold was lifted, and the flow table was initiated. Following 25 vibrations of the flow table, the average diameter of the vertical two directions was tested as the final result. The test process is shown in Fig. 4.

The setting time according to GB/T 1346–2011, using a standard Vicat instrument (China, Shaoxing Exploration Instrument Factory) test. The prepared slurry was poured into the mold. The initial setting needle is immersed into the slurry from a height close to the surface of the slurry. When the test needle is 4 ± 1 mm away from the bottom of the mold and no longer sinks, the slurry reaches the initial

setting state. Subsequently, the mold was flipped, and the slurry was deemed to have reached the final setting state when the final setting needle sank to a distance less than 5 mm into the slurry.

Mechanical properties

According to GB/T 17,671–2021, using WAW-1000 pressure testing machine (China, Shanghai Hualong Testing Instrument Co., Ltd.), the prism sample with a size of 40 mm × 40 mm × 160 mm was broken from the middle part and the compressive strength test was carried out. The results are valid averages of at least six samples.

Hydration

The main phase composition was tested by XRD. The instrument used is the D8 Advance X-ray diffractometer (Bruker, Germany). The operating voltage and current are 45 Kv and 40 mA respectively. The scanning range and speed are 5–70° 2θ and 5°/min respectively. The material functional groups and element bonding of the samples were analyzed by Fourier transform infrared spectroscopy (FTIR). The instrument used is a Nicolet iS50 FTIR Spectrometer, using a conventional KBr tablet test, test wave number range of 400–4000 cm^{-1}. The microstructure of the samples was analyzed by SEM and energy dispersive spectroscopy (EDS). The instrument used was Zeiss Gemini 300. Before testing, samples underwent slicing, resulting in a diameter of $\leq$1 cm and a thickness < 1 cm. The smooth surface was selected as the test surface. Subsequently, the sample surface was sprayed with gold (30 mA, 150 s) and put into the instrument for vacuum treatment.

Results and discussion

Fluidity

Figure 5 shows the AAPGF fluidity test results. According to the requirements of GB 175–2007, the fluidity should not be less than 180 mm. All groups, except for the PGF-0 group meet this requirement, and the addition of GBFS/FA has a good improvement effect on the fluidity of AAPGF.
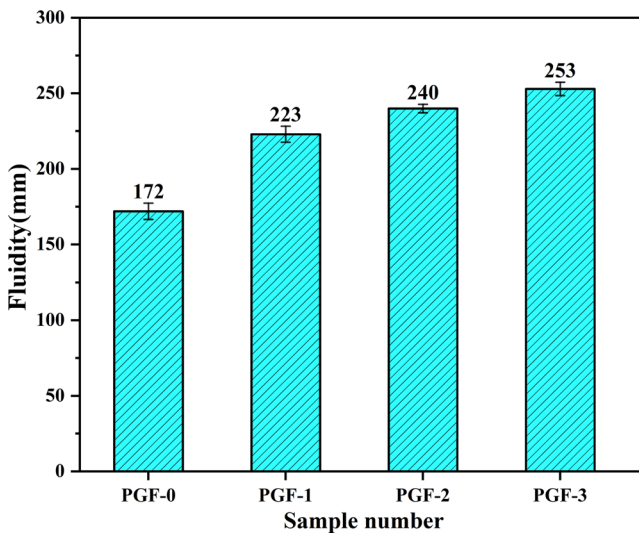
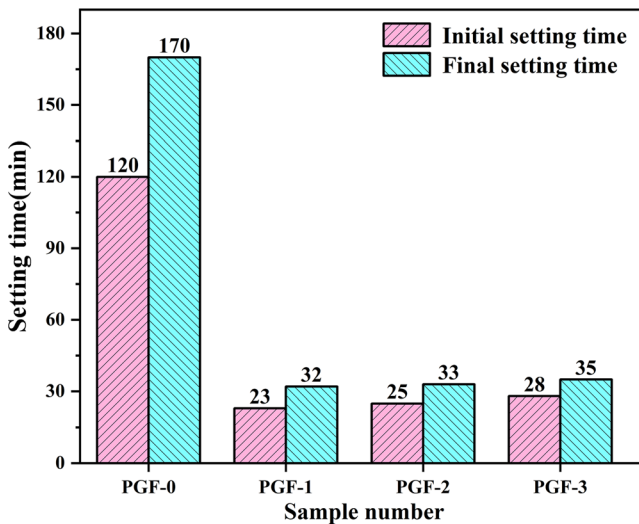**Fig. 5** AAPGF fluidity test results with different GBFS/FA contents

Fig. 6 AAPGF setting time test results with different GBFS/FA contents

Fig. 7 AAPGF compressive strength test results with different GBFS/FA contents

As seen from the SEM image of PS, the PS particles have irregular shapes, more angular particles and larger particle size (D50 = 20.52 μm), which increases the friction between particles, thus the PGF-0 group has the lowest fluidity. Compared with PS, GBFS (D50 = 10.6 μm) and FA (D50 = 8.92 μm) have smaller particle sizes. They are distributed between PS particles, thereby improving the particle size distribution of AAPGF and enhancing its fluidity [38].

In addition, although the high amorphous phase content of GBFS can increase the early reaction rate and accelerate the consumption of mixed water, thereby reducing fluidity [39]. However, FA exhibits minimal involvement in the reaction during the early s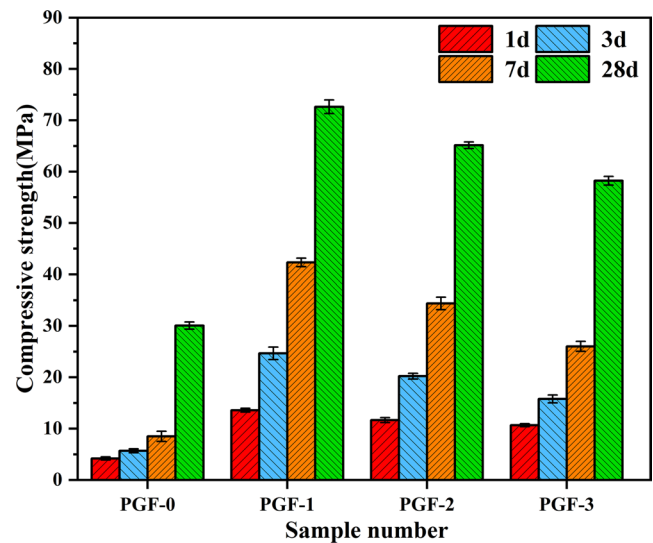tages. The angular-free spherical particles can exert a morphological effect [40] and play a leading role in enhancing fluidity [41].

Setting time

Figure 6 shows the AAPGF setting time test outcomes. The incorporation of GBFS/FA greatly shortens the setting time of AAPGF leading to flash setting.

This phenomenon is mainly related to the rapid dissolution of GBFS in an alkaline solution. GBFS swiftly dissolve the necessary Ca^{2+} ions for the reaction in the alkaline solution, providing more nucleation sites for the remaining dissolved substances [24]. This process promotes the formation of C-(A)-S-H gel, accelerate the hydration reaction, and shorten the setting time. It is found that the incorporation of FA into GBFS can improve the flash setting phenomenon caused by GBFS [42]. However, even with a 30% FA content in AAPGF, the flash setting phenomenon has not been alleviated. This is attributed to both PS and GBFS in AAPGF have higher CaO content, so the hydration reaction rate at room temperature is higher than that of FA [43, 44]. Consequently, a certain amount of FA has limited impact on the setting time.

Compressive strength

Figure 7 shows the results of the compressive strength tests for AAPGF. The compressive strength of the PGF-0 group stimulated by PS alone was lower. The compressive strength from 1 day–28 days was 4.2 MPa, 5.7 MPa, 8.51 MPa and 30.09 MPa, respectively. Significantly lagging behind other groups. Moreover, due to the presence of P_2O_5 in PS, the

early strength development in the PGF-0 group was slower than that in the later period.

The presence of P_2O_5 results in the generation soluble phosphate ions (PO_4^{3-}) in the solution. When PO_4^{3-} reacts with Ca^{2+} ions, it forms insoluble substances, reduce the concentration of Ca^{2+} ions, and adhering to the surface of the particles [45]. This process adversely affects the normal progress of the hydration reaction. Moreover, the lack of Al element in PS is also one of the factors causing the low strength of PGF-0 group. Following the incorporation of GBFS/FA, the compressive strength of the PGF-1–PGF3 group was significantly improved. This enhancement is attributed to the ability of GBFS to rapidly dissolve Ca^{2+} and Al^{3+} ions in an alkaline solution, forming C-(A)-S-H gel. This can not only reduce the adverse effects of P_2O_5, but also supplement Al element for AAPGF, thus ensuring the development of strength.

The PGF-1 group, with a 30% GBFS/FA content, exhibited the highest strength, reaching 72.65 MPa at 28 days. However, when the content of GBFS/FA is more than 30%, the compressive strength of each age decreases. This is related to the increase in the proportion of FA substituted PS in AAPGF. The activity of FA is low, and it basically exists in the form of filler in the system. Over time, although some active substances can precipitate Si^{4+} and Al^{3+} ions to form N-A-S-H gel [46], the number of its formation is extremely limited at room temperature, and most of them still exist in the form of inert filler. On the contrary, despite the relatively slow early reaction of PS, it gradually dissolves and form C-S-H gel in the later stage of hydration [21], ensuring the growth of strength. This also proves that in AAPGF, the hydration activity of PS is greater than that of FA.
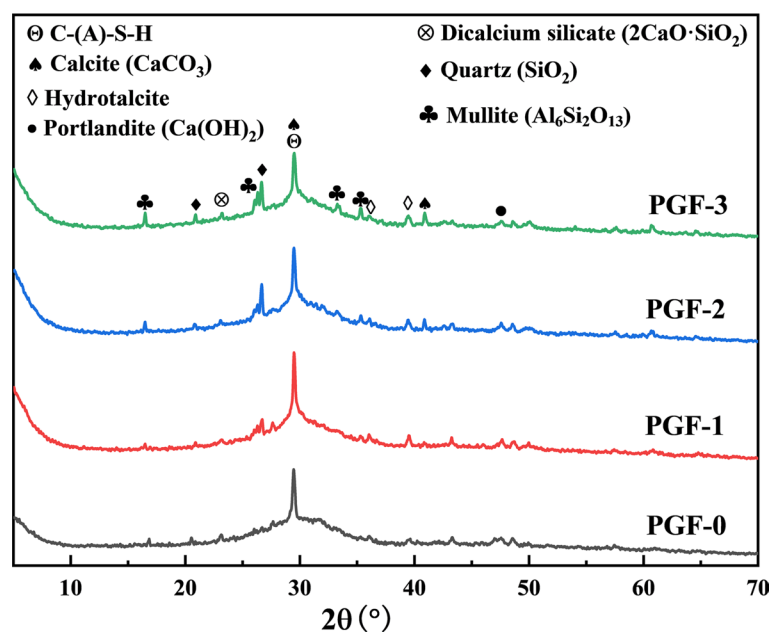
XRD analysis

Figure 8 shows the XRD results of AAPGF. The primary phases identified encompass C-(A)-S-H gel, Portlandite, hydrotalcite and phase composition in raw materials. The N-A-S-H gel exhibits amorphous properties [47], and consequently, no relevant characteristic peaks were found in the XRD spectrum.

There is a broad hump in each group near 20–35° 2θ, indicating that there is an amorphous phase. Part of the amorphous phase is derived from raw materials, and the other part is newly generated by hydration reaction [48]. The addition of GBFS/FA does not significantly alter the hump area, so the strength difference could not be evaluated by the amorphous phase content. There are obvious C-(A)-S-H gel characteristic peaks in each group near 29° 2θ. The existence of C-(A)-S-H gel peak in PGF-0 group confirmed the hydration ability of PS in the later stage. Following the adding GBFS/FA, the C-(A)-S-H gel peak was enhanced, with the peak value reaching its maximum in the PGF-1 group. The Ca^{2+} and Al^{3+} ions decomposed from GBFS promoted the formation of C-(A)-S-H gel. However, with the increase of the proportion of low activity FA replacing PS, the C-(A)-S-H gel characteristic peaks in PGF-2 and PGF-3 groups gradually weakened, which was consistent with the strength test results.

In addition, unlike the PGF-0 group, a new crystal peak of hydrotalcite was found in PGF-1–PGF-3 groups. Hydrotalcite is the hydration product of Mg, Al and carbonate (CO_3^{2-}) [47], forms due to the active Mg and Al elements present in GBFS/FA. Consequently, the incorporation of GBFS/FA improves the compressive strength by augmenting the number of gels such as C-(A)-S-H and hydrotalcite.

Fig. 8 XRD patterns of AAPGF 28 at days with different GBFS/FA contents

In addition, with the increase of FA substitution ratio in AAPGF, the mullite and quartz phase gradually become obvious. This suggests that these two phases are relatively stable and not easy to react with other substances.

FTIR analysis

Figure 9 shows the FTIR results of AAPGF. There is a broad peak at 980–1001 cm^{-1} corresponding to the antisymmetric stretching vibration of Si-O-T (T = Si, Al) bonds in the gel [49]. In comparison to the PGF-0 group, the wave number of the PGF-1–PGF-3 group decreased from 1001 cm^{-1} to 980 cm^{-1}. The Al-O bond has a lower vibrational frequency than the Si-O bond [50], the decrease of wavenumber indicates a greater substitution of Si by Al in the reaction product, leading to the formation of more Al-containing gels.

It has been observed that when the wavenumber of the system is higher than that of C-A-S-H gel (950 cm^{-1}) and lower than that of N-A-S-H gel (1020 cm^{-1}), there were many types of gel products [28]. The wave number of the PGF-1–PGF-3group shifted from 980 cm^{-1} to 996 cm^{-1}, and the wave number increased continuously and approached 1020 cm^{-1}. This trend suggests an augmented production of N-A-S-H gels. Usually, the SiO_4 tetrahedra in the gel have Q^n units ($n = 0$–4) due to the different numbers of bridging oxygen. The wave numbers of Q^0–Q^4 are located near 850 cm^{-1},900 cm^{-1},950 cm^{-1},1100 cm^{-1} and 1200 cm^{-1}, respectively [51]. The PGF-0–PGF-3 group produced an absorption peak near 950 cm^{-1}, signifying that the SiO_4 tetrahedron in the product C-(N)-A-S-H gel mainly existed in the form of Q^2 unit.

The band peaks near 1640 cm^{-1} and 3450 cm^{-1} are related to the bending vibration and tensile vibration of O-H in crystal water, respectively [52]. Compared with the PGF-0 group, the PGF-1 group exhibited the largest peak

area and the highest strength, indicating that the most hydration products were generated. However, a notable reduction was observed in the PGF-2 and PGF-3 groups, attributed to the formation of N-A-S-H gel with low bound water content [53]. The band peaks near 1424 cm^{-1} and 874 cm^{-1} were related to the asymmetric tensile vibration of the O-C-O bond, indicating the occurrence of the carbonization reaction [51]. The band peak at 713 cm^{-1} is the bending vibration of the Si-O-Al bond induced by the substitution of Si by tetracoordinate aluminum [Al (IV)] [54]. This observation further confirms the presence of Al-containing gel in the hydration product. Additionally, the band peak near 456 cm^{-1} is caused by the bending vibration of the Si-O-Si bond and Si-O bond in the hydration product gel [55].

SEM-EDS analysis

Figure 10 is the SEM image of AAPGF. In the PGF-0 group, unhydrated PS particles with angular shape are observable, and the number of hydration products is limited, with insufficient overlap. Simultaneously, a certain number of pores are evident. Upon the addition of GBFS/FA, it is difficult to observe the presence of unhydrated particles in the PGF-1–PGF-3 group. Moreover, more large-sized hydration products are formed around the particles. This observation indicates that GBFS/FA can promote the dissolution of PS and increase the number of hydration products. However, it is noted that some large pores are evident in the group mixed with GBFS/FA. This is related to the high activity of GBFS in the early stage of hydration, resulting in uneven distribution of hydration products and subsequently increasing the gap between particles [37].

The EDS energy spectrum data of AAPGF at 28 days are shown in Table 3 representing the average values from six points in different regions. The chemical composition
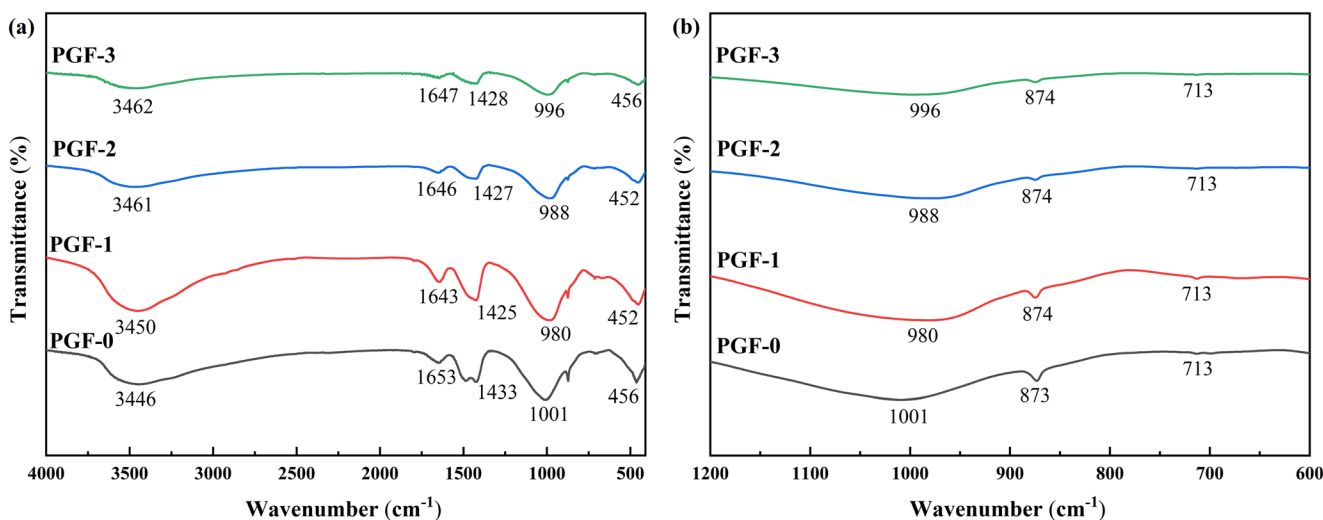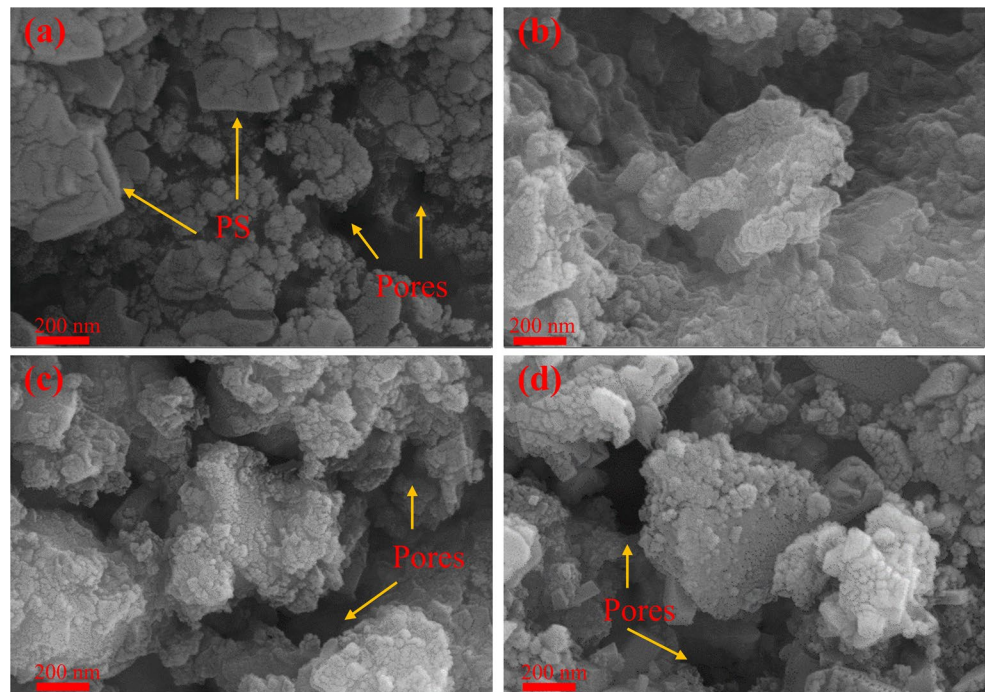

Fig. 9 FTIR spectra of AAPGF at 28 days with different GBFS/FA contents: (**a**) 400–4000 cm^{-1} and (**b**) 600–1200 cm^{-1}

Fig. 10 SEM images of AAPGF at 28 days with different GBFS/FA contents: (**a**) PGF-0, (**b**) PGF-1, (**c**) PGF-2, and (**d**) PGF-3

Table 3 EDS energy spectrum data of AAPGF at 28 days (at%)

Specimens	Ca	Si	Al	Na	Ca/Si	Si/Al	Na/Ca
P-0	15.61	9.97	0.86	2.70	1.57	11.59	0.17
PGF-1	7.21	10.19	2.20	2.80	0.71	4.63	0.39
PGF-2	6.65	9.47	3.54	2.68	0.70	2.68	0.40
PGF-3	5.61	11.37	5.19	2.57	0.49	2.19	0.46

of the hydration products is mainly composed of Ca, Si, Al and Na. The presence of these elements confirms the co-existence of C-(N)-A-S-H gel and N-A-S-H gel in AAPGF [34], which is consistent with the FTIR results. The element distribution in the PGF-0 group is mainly composed of Ca and Si elements, with minimal Na and Al elements, indicating that the hydration products at this time are mainly C-S-H gel. Following the addition of GBFS/FA, both the Ca/Si ratio and Si/Al ratio gradually decreased, and the Na/Ca ratio gradually increased. The increase of the proportion of GBFS/FA replacing PS will gradually reduce the concentration of Ca^{2+} ions and an increased release of Al-O bonds. In response, Na^+ ions are adsorbed into the Si-O-Al bond, forming C-(N)-A-S-H and N-A-S-H gels with a high degree of polymerization to balance the charge [56].

Conclusion

To make effective use of PS solid waste, AAPGF was prepared by using PS and GBFS/FA as precursors. The effects of different GBFS/FA contents on the workability performance, mechanical properties and hydration products of AAPGF were investigated. The conclusions are as follows:

1. GBFS/FA increases fluidity by optimizing the particle distribution of AAPGF and exerting morphological effects. Due to the high activity of GBFS, a large amount of C-(A)-S-H gel can be generated in the early stage of hydration, resulting in the flash setting of AAPGF, and the increase of FA ratio cannot alleviate the flash setting caused by GBFS.

2. GBFS/FA increases the strength of AAPGF. When the replacement ratio is 30%, the 28 days strength can reach the highest 72.65 MPa. PS can react to form C-S-H gel in the later stage of hydration, so the increase of the proportion of FA replacing PS leads to the decrease of compressive strength.

3. GBFS/FA increased the amount of C-(A)-S-H gel in AAPGF, accompanied by the formation of hydrotalcite gel. In addition, GBFS/FA also increases the content of Al and Na elements, transforms the hydration products from C-S-H gel to C-(N)-A-S-H and N-A-S-H gel, and improves the degree of polymerization. The SiO_4 tetrahedron mainly exists in the form of Q^2 unit.

4. GBFS/FA significantly reduced the number of unhydrated AAPGF particles. However, the high activity of GBFS in the early stage will lead to uneven distribution of hydration products and the formation of large pores.

Declarations

Ethical approval This study is mainly in the field of civil engineering materials. Biological experiments on animals or humans were not involved. Therefore, this article does not require ethical approval.

Consent to participate All the authors of this study have agreed to publish. Ensure that the manuscript content is original and not considered to be published in other places.

Consent for publication Not applicable.

Conflict of interest The authors declare no competing interests.

References

1. Zhang, Y., Li, Z., Gu, X., Nehdi, M.L., Marani, A., Zhang, L.: Utilization of iron ore tailings with high volume in green concrete. J. Build. Eng. **72**, 106585 (2023). https://doi.org/10.1016/j.jobe.2023.106585

2. Ren, Z., Wang, L., Wang, H., Liu, S., Ren, J.: Stabilization and solidification mechanism of pb in phosphogypsum slag-based cementitious materials. Constr. Build. Mater. **368**, 130427 (2023). https://doi.org/10.1016/j.conbuildmat.2023.130427

3. Shi, C., Jiménez, A.F., Palomo, A.: New cements for the 21st century: The pursuit of an alternative to Portland cement. Cem. Concr Res. **41**, 750–763 (2011). https://doi.org/10.1016/j.cemconres.2011.03.016

4. Luukkonen, T., Abdollahnejad, Z., Yliniemi, J., Kinnunen, P., Illikainen, M.: One-part alkali-activated materials: A review. Cem. Concr Res. **103**, 21–34 (2018). https://doi.org/10.1016/j.cemconres.2017.10.001

5. Ng, C., Alengaram, U.J., Wong, L.S., Mo, K.H., Jumaat, M.Z., Ramesh, S.: A review on microstructural study and compressive strength of geopolymer mortar, paste and concrete. Constr. Build. Mater. **186**, 550–576 (2018). https://doi.org/10.1016/j.conbuildmat.2018.07.075

6. Ruiz-Santaquiteria, C., Skibsted, J., Fernández-Jiménez, A., Palomo, A.: Alkaline solution/binder ratio as a determining factor in the alkaline activation of aluminosilicates. Cem. Concr Res. **42**, 1242–1251 (2012). https://doi.org/10.1016/j.cemconres.2012.05.019

7. Gao, X., Yao, X., Yang, T., Zhou, S., Wei, H., Zhang, Z.: Calcium carbide residue as auxiliary activator for one-part sodium carbonate-activated slag cements: Compressive strength, phase assemblage and environmental benefits. Constr. Build. Mater. **308**, 125015 (2021). https://doi.org/10.1016/j.conbuildmat.2021.125015

8. Aliabdo, A.A., Elmoaty, A., Emam, A.E.M.: Factors affecting the mechanical properties of alkali activated ground granulated blast furnace slag concrete. Constr. Build. Mater. **197**, 339–355 (2019). https://doi.org/10.1016/j.conbuildmat.2018.11.086

9. Lee, T., Li, Z.: Conditioned MSWI ash-slag-mix as a replacement for cement in cement mortar. Constr. Build. Mater. **24**, 970–979 (2010). https://doi.org/10.1016/j.conbuildmat.2009.11.021

10. You, N., Li, B., Cao, R., Shi, J., Chen, C., Zhang, Y.: The influence of steel slag and ferronickel slag on the properties of alkali-activated slag mortar. Constr. Build. Mater. **227**, 116614 (2019). https://doi.org/10.1016/j.conbuildmat.2019.07.340

11. Zhao, Y., Yang, C., Li, K., Qu, F., Yan, C., Wu, Z.: Toward understanding the activation and hydration mechanisms of composite activated coal gangue geopolymer. Constr. Build. Mater. **318**, 125999 (2022). https://doi.org/10.1016/j.conbuildmat.2021.125999

12. Tchadjié, L.N., Ekolu, S.O., Quainoo, H., Tematio, P.: Incorporation of activated bauxite to enhance engineering properties and microstructure of volcanic ash geopolymer mortar composites. J. Build. Eng. **41**, 102384 (2021). https://doi.org/10.1016/j.jobe.2021.102384

13. Gultekin, A., Yazici, S., Ramyar, K.: Effect of trass calcination on properties of geopolymer mixtures. J. Aust Ceram. Soc. **58**, 1623–1631 (2022). https://doi.org/10.1007/s41779-022-00799-y

14. Hossain, M.M., Karim, M.R., Elahi, M.M.A., Islam, M.N., Zain, M.F.M.: Long-term durability properties of alkali-activated binders containing slag, fly ash, palm oil fuel ash and rice husk ash. Constr. Build. Mater. **251**, 119094 (2020). https://doi.org/10.1016/j.conbuildmat.2020.119094

15. Andrejkovičová, S., Patinha, C., Silva, E.F., Rocha, F.: The effect of natural zeolite on microstructure, mechanical and heavy metals adsorption properties of metakaolin based geopolymers. Appl. Clay Sci. **126**, 141–152 (2016). https://doi.org/10.1016/j.clay.2016.03.009

16. Jiang, X., Xiao, R., Zhang, M., Hu, W., Bai, Y., Huang, B.: A laboratory investigation of steel to fly ash-based geopolymer paste bonding behavior after exposure to elevated temperatures. Constr. Build. Mater. **254**, 119267 (2020). https://doi.org/10.1016/j.conbuildmat.2020.119267

17. Yu, H., Li, S., Qian, G., Gong, X., Wang, K.: Experiment evaluation on the surface treatment of phosphorus slag (PS) micropowder for asphalt modification. Constr. Build. Mater. **262**, 119931 (2020). https://doi.org/10.1016/j.conbuildmat.2020.119931

18. Xie, F., Liu, Z., Zhang, D., Wang, J., Wang, D., Ni, J.: The effect of NaOH content on rheological properties, microstructures and interfacial characteristic of alkali activated phosphorus slag fresh pastes. Constr. Build. Mater. **252**, 119132 (2020). https://doi.org/10.1016/j.conbuildmat.2020.119132

19. Xie, F., Liu, Z., Zhang, D., Wang, J., Huang, T., Wang, D.: Reaction kinetics and kinetics models of alkali activated phosphorus slag. Constr. Build. Mater. **237**, 117728 (2020). https://doi.org/10.1016/j.conbuildmat.2019.117728

20. Wang, L., Guo, F., Lin, Y., Yang, H., Tang, S.W.: Comparison between the effects of phosphorous slag and fly ash on the C-S-H structure, long-term hydration heat and volume deformation of cement-based materials. Constr. Build. Mater. **250**, 118807 (2020). https://doi.org/10.1016/j.conbuildmat.2020.118807

21. Zhang, Z., Wang, Q., Yang, J.: Hydration mechanisms of composite binders containing phosphorus slag at different temperatures. Constr. Build. Mater. **147**, 720–732 (2017). https://doi.org/10.1016/j.conbuildmat.2017.04.202

22. Jia, R., Wang, Q., Luo, T.: Investigation of the relationship among the hydration, microstructure and compressive strength of alkali-activated phosphorus slag. J. Build. Eng. **76**, 107293 (2023). https://doi.org/10.1016/j.jobe.2023.107293

23. Maghsoodloorad, H., Khalili, H., Allahverdi, A.A.: Alkaliactivated Phosphorous Slag performance under different curing conditions: Compressive strength, Hydration products, and microstructure. J. Mater. Civ. Eng. **30**, 4017253 (2018). https://doi.org/10.1061/(ASCE)MT.1943-5533.0002101

24. Shah, S.F.A., Chen, B., Oderji, S.Y., Haque, M.A., Ahmad, M.R.: Improvement of early strength of fly ash-slag based one-part alkali activated mortar. Constr. Build. Mater. **246**, 118533 (2020). https://doi.org/10.1016/j.conbuildmat.2020.118533

25. Yu, T., Chen, J., Guo, H., Zhang, B., He, X., Zheng, A., Wang, Q., Yuan, P.: Mechanical properties and microstructure of ground granulated blast furnace slag-based geopolymer reinforced with polyvinyl alcohol fibers. J. Mater. Cycles Waste Manag. **25**, 1719–1731 (2023). https://doi.org/10.1007/s10163-023-01646-3

26. Aiken, T.A., Kwasny, J., Sha, W., Tong, K.T.: Mechanical and durability properties of alkali-activated fly ash concrete with increasing slag content. Constr. Build. Mater. **301**, 124330 (2021). https://doi.org/10.1016/j.conbuildmat.2021.124330

27. Fang, G., Ho, W.K., Tu, W., Zhang, M.: Workability and mechanical properties of alkali-activated fly ash-slag concrete cured at ambient temperature. Constr. Build. Mater. **172**, 476–487 (2018). https://doi.org/10.1016/j.conbuildmat.2018.04.008

28. Sun, R., Fang, C., Zhang, H., Ling, Y., Feng, J., Qi, H., Ge, Z.: Chemo-mechanical properties of alkali-activated slag/fly ash paste incorporating white mud. Constr. Build. Mater. **291**, 123312 (2021). https://doi.org/10.1016/j.conbuildmat.2021.123312

29. Huseien, G.F., Sam, A.R.M., Shah, K.W., Asaad, M.A., Tahir, M.M., Mirza, J.: Properties of ceramic tile waste based alkaliactivated mortars incorporating GBFS and fly ash. Constr. Build. Mater. **214**, 355–368 (2019). https://doi.org/10.1016/j.conbuildmat.2019.04.154

30. Song, W., Zhu, Z., Pu, S., Wan, Y., Huo, W., Song, S., Zhang, J., Yao, K., Hu, L.: Efficient use of steel slag in alkali-activated fly ash-steel slag-ground granulated blast furnace slag ternary blends. Constr. Build. Mater. **259**, 119814 (2020). https://doi.org/10.1016/j.conbuildmat.2020.119814

31. Haddad, R.H., Ashteyat, A.M., Lababneh, Z.K.: Producing geopolymer composites using oil shale ash. Struct. Concr. **20**, 225–235 (2019). https://doi.org/10.1002/suco.201800007

32. Caldas, P.H.C.H., de Azevedo, A.R.G., Marvila, M.T.: Silica fume activated by NaOH and KOH in cement mortars: Rheological and mechanical study. Constr. Build. Mater. **400**, 132623 (2023). https://doi.org/10.1016/j.conbuildmat.2023.132623

33. Liu, Z., Ni, W., Li, Y., Ba, H., Li, N., Ju, Y., Zhao, B., Jia, G., Hu, W.: The mechanism of hydration reaction of granulated blast furnace slag-steel slag-refining slag-desulfurization gypsum-based clinker-free cementitious materials. J. Build. Eng. **44**, 103289 (2021). https://doi.org/10.1016/j.jobe.2021.103289

34. Yousefi Oderji, S., Chen, B., Ahmad, M.R., Shah, S.F.A.: Fresh and hardened properties of one-part fly ash-based geopolymer binders cured at room temperature: Effect of slag and alkali activators. J. Clean. Prod. **225**, 1–10 (2019). https://doi.org/10.1016/j.jclepro.2019.03.290

35. Xiang, J., He, Y., Cui, X., Liu, L.: Enhancement of setting times and hardening of alkali-activated slag binder using CO2-modified slag. Cem. Concr. Compos. **134**, 104797 (2022). https://doi.org/10.1016/j.cemconcomp.2022.104797

36. Marvila, M.T., De Azevedo, G., Linhares, A.R.T., Júnior, J.A., Fontes Vieira, C.M.: Activated alkali cement based on blast furnace slag: Effect of curing type and concentration of Na2O. J. Mater. Res. Technol. **23**, 4551–4565 (2023). https://doi.org/10.1016/j.jmrt.2023.02.088

37. Zhang, Y., Yang, D., Wang, Q.: Performance study of alkali-activated phosphate slag-granulated blast furnace slag composites: Effect of the granulated blast furnace slag content. Arch. Civ. Mech. Eng. **23** (2023). https://doi.org/10.1007/s43452-023-00724-5

38. Wang, Q., Cui, X., Wang, J., Li, S., Lv, C., Dong, Y.: Effect of fly ash on rheological properties of graphene oxide cement paste. Constr. Build. Mater. **138**, 35–44 (2017). https://doi.org/10.1016/j.conbuildmat.2017.01.126

39. Kamath, M., Prashant, S., Kumar, M.: Micro-characterisation of alkali activated paste with fly ash-GGBS-metakaolin binder system with ambient setting characteristics. Constr. Build. Mater. **277**, 122323 (2021). https://doi.org/10.1016/j.conbuildmat.2021.122323

40. Dong, D., Huang, Y., Pei, Y., Zhang, X., Cui, N., Zhao, P., Hou, P., Lu, L.: Effect of spherical silica fume and fly ash on the rheological property, fluidity, setting time, compressive strength, water resistance and drying shrinkage of magnesium ammonium phosphate cement. J. Build. Eng. **63**, 105484 (2023). https://doi.org/10.1016/j.jobe.2022.105484

41. Zhang, X., Wang, W., Zhang, Y., Gu, X.: Research on hydration characteristics of OSR-GGBFS-FA alkali-activated materials. Constr. Build. Mater. **411**, 134321 (2024). https://doi.org/10.1016/j.conbuildmat.2023.134321

42. Nedunuri, A.S.S.S., Muhammad, S.: Fundamental understanding of the setting behaviour of the alkali activated binders based on ground granulated blast furnace slag and fly ash. Constr. Build. Mater. **291**, 123243 (2021). https://doi.org/10.1016/j.conbuildmat.2021.123243

43. Wang, Y., Xiao, R., Hu, W., Jiang, X., Zhang, X., Huang, B.: Effect of granulated phosphorus slag on physical, mechanical and microstructural characteristics of Class F fly ash based geopolymer. Constr. Build. Mater. **291**, 123287 (2021). https://doi.org/10.1016/j.conbuildmat.2021.123287

44. Hojati, M., Radlińska, A.: Shrinkage and strength development of alkali-activated fly ash-slag binary cements. Constr. Build. Mater. **150**, 808–816 (2017). https://doi.org/10.1016/j.conbuildmat.2017.06.040

45. Lee, N.K., Lee, H.K.: Setting and mechanical properties of alkali-activated fly ash/slag concrete manufactured at room temperature. Constr. Build. Mater. **47**, 1201–1209 (2013). https://doi.org/10.1016/j.conbuildmat.2013.05.107

46. Shang, J., Dai, J., Zhao, T., Guo, S., Zhang, P., Mu, B.: Alternation of traditional cement mortars using fly ash-based geopolymer mortars modified by slag. J. Clean. Prod. **203**, 746–756 (2018). https://doi.org/10.1016/j.jclepro.2018.08.255

47. Rafeet, A., Vinai, R., Soutsos, M., Sha, W.: Effects of slag substitution on physical and mechanical properties of fly ash-based alkali activated binders (AABs). Cem. Concr Res. **122**, 118–135 (2019). https://doi.org/10.1016/j.cemconres.2019.05.003

48. Fan, J., Zhu, H., Shi, J., Li, Z., Yang, S.: Influence of slag content on the bond strength, chloride penetration resistance, and interface phase evolution of concrete repaired with alkali activated slag/fly ash. Constr. Build. Mater. **263**, 120639 (2020). https://doi.org/10.1016/j.conbuildmat.2020.120639

49. Jia, R., Wang, Q., Luo, T.: Understanding the workability of alkali-activated phosphorus slag pastes: Effects of alkali dose and silicate modulus on early-age hydration reactions. Cem. Concr. Compos. **133**, 104649 (2022). https://doi.org/10.1016/j.cemconcomp.2022.104649

50. Zhang, S., Keulen, A., Arbi, K., Ye, G.: Waste glass as partial mineral precursor in alkali-activated slag/fly ash system. Cem. Concr Res. **102**, 29–40 (2017). https://doi.org/10.1016/j.cemconres.2017.08.012

51. Liu, Z., Zhang, D., Li, L., Wang, J., Shao, N., Wang, D.: Microstructure and phase evolution of alkali-activated steel slag during early age. Constr. Build. Mater. **204**, 158–165 (2019). https://doi.org/10.1016/j.conbuildmat.2019.01.213

52. Liu, Z., Hu, G.: The mechanism of hydration reaction of granulated blast furnace slag-steel slag-refining slag-desulfurization gypsum-based clinker-free cementitious materials. J. Build. Eng. **44**, 103289 (2021). https://doi.org/10.1016/j.jobe.2021.103289

53. Ma, H., Wu, C.: Mechanical and microstructural properties of alkali-activated fly ash-slag material under sustained moderate temperature effect. Cem. Concr. Compos. **134**, 104744 (2022). https://doi.org/10.1016/j.cemconcomp.2022.104744

54. Ma, H., Chen, J., Xu, H., Wang, X.: Preparation and reaction mechanism characterization of Alkali-activated coal gangue–slag materials. Materials. **12**, 2250 (2019). https://doi.org/10.3390/ma12142250

55. Zhang, Z., Wong, Y.C., Arulrajah, A., Sofi, M., Sabri, Y.: Reaction mechanism of alkali-activated brick clay mill residues. Constr. Build. Mater. **341**, 127817 (2022). https://doi.org/10.1016/j.conbuildmat.2022.127817

56. Sakulich, A.R., Anderson, E., Schauer, C., Barsoum, M.W.: Mechanical and microstructural characterization of an alkali-activated slag/limestone fine aggregate concrete. Constr. Build. Mater. **23**, 2951–2957 (2009). https://doi.org/10.1016/j.conbuildmat.2009.02.022